PREDICTION CAPABILITIES OF MAXIMUM LIFT EFFECTS FOR REALISTIC HIGH-LIFT-COMMERCIAL-AIRCRAFT-CONFIGURATIONS WITHIN THE EUROPEAN PROJECT EUROLIFT II

H. Frhr. von Geyr, N. Schade
German Aerospace Center (DLR), Institute of Aerodynamics and Flow Technology
Lilienthalplatz 7, 38108 Braunschweig
Germany

OVERVIEW

Within the framework of the European project EUROLIFT II extensive numerical computations have been conducted aiming to assess the capabilities of CFD to predict the dependence of the high-lift performance on the Reynolds number and to further improve the understanding of the high-lift associated vortex phenomena, especially the nacelle strake mechanism. These computations have been conducted by five European partners within the EUROLIFT II project. A cross-comparison of these results can be found in reference [1]. Within this paper the focus is put on continuative analysis of the results based on the computations performed by the authors. The paper will outline the validation activities, based on LSWT and ETW wind tunnel measurements, forming the base for the assessment of the prediction capabilities conform to the objectives. Additional results will be presented addressing the influence of the computational grid on the predicted high-lift performance.

NOMENCLATURE

α	=	Angle of attack in degrees
Cp	=	Pressure coefficient
c_{fx}	=	Component of the projected skin friction tensor in the x direction
C_L	=	Lift coefficient
C_D	=	Drag coefficient
Ma	=	Mach number
Re	=	Reynolds number
μ_t	=	Turbulent dynamic viscosity

1. INTRODUCTION

The three-element high-lift system of commercial transport aircraft (slat, main wing and Fowler-type of flap) is well established with a very efficient compromise between the gain of lift and the complexity of the mechanical system. The principle interaction mechanisms between the three elements are understood and presented in detail in reference [2]. However, the geometry of realistic high-lift systems is more complicated and the interaction mechanisms are disturbed by vortex flows. The appearance of vortices is geometrically conditioned. Such vortices are generated by the sharp edges and affect the high-lift flow behavior of the configuration. For instance, the aerodynamic requirement of a clean transition of the wing leading edge to the fuselage at cruise conditions on one side and the deflection of the slat at high-lift conditions lead to the geometrical consequence of an Onglet. When the slat is extended, parts of this Onglet form a slat horn. The underwing engine installation leads to an even more complex situation. The deflection of the slat is interrupted at the position of the pylon, adding vortices to the flow field generated by the flanges of the slat cut-out. This slat cut-out in region of the engine and the presence of the engine lead to a significant loss of maximum lift compared to the high-lift configuration without engine. In order to recover these lift losses at least partially, strakes may be placed on the nacelle.

Within the European project EUROLIFT II one of the main goals is the improvement of the understanding of the vortex developments and interactions associated with the high-lift flow field at maximum lift. To be able to study these phenomena systematically the complexity level of the EUROLIFT (I) KH3Y configuration is gradually increased in three steps towards a realistic configuration of modern commercial transport aircraft. Within EUROLIFT (I) the base geometry consists of a fuselage, a flap and a continuous slat. Slat tracks and flap tracks have been neglected. Within EUROLIFT (II) this configuration was equipped with a slat horn, an Onglet, slat tracks, pressure tube bundles, and flap track fairings (FTF), representing the Stage 1 configuration. The adding of a through-flow nacelle and a pylon leads to the Stage 2 configuration. For the third, the most complex Stage 3 configuration, a nacelle strake was added. In Figure 1 all three configurations are shown with the geometrical differences marked in color.

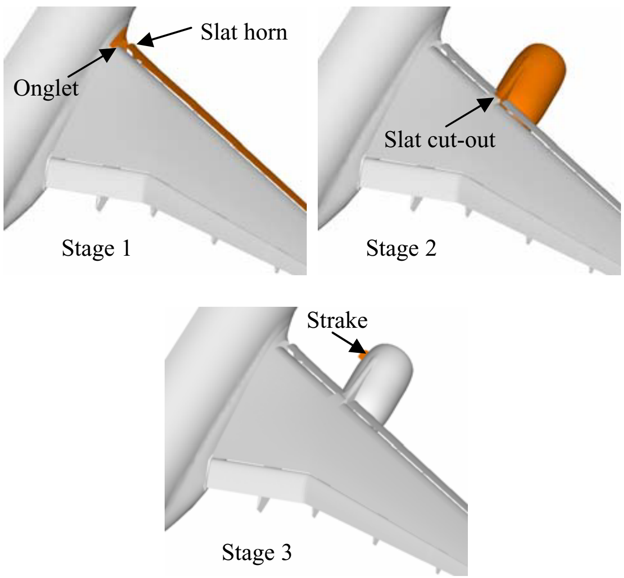

FIG 1. Extension Stages of the KH3Y-configuration towards a realistic high-lift aircraft configuration.

Within EUROLIFT II comprehensive wind tunnel measurements in the Low Speed Wind Tunnel (LSWT) of Airbus Deutschland as well as in the European Transonic Wind tunnel (ETW) in Cologne, Germany, have been conducted for all three Stages at Reynolds number ranging from $Re=1.33 \cdot 10^6$ up to $Re=25 \cdot 10^6$. The results of these measurements serve as a comprehensive database used to validate the numerical methods.

High-Lift computations for such highly complex configurations are very challenging and not yet a standard application. Within EUROLIFT II DLR performed polar computations for all three Stages for three different Reynolds-numbers. The key objectives are to assess the assess the capabilities of CFD to capture maximum lift, to capture the Reynolds-number dependence of maximum lift and to analyze the vortex phenomena associated with the high-lift flows of the different configurations in order to improve the understanding of the dominant effects. Of special interest are the associated stall mechanisms and the strake effect.

2. STRATEGY FOR GRID GENERATION

All configurations as sketched in Figure 1 have been generated based on the KH3Y-configuration using CATIA V5[3]. In [5] it is shown that even small geometrical details such as the slat tracks and the pressure tube bundles reduce maximum lift. The pressure tube bundles are located aside of each slat track and are basically a bundle of single pressure tubes which connect the pressure measurement holes on the slat with the transducers. The following figure shows the location of the pressure tube bundles.

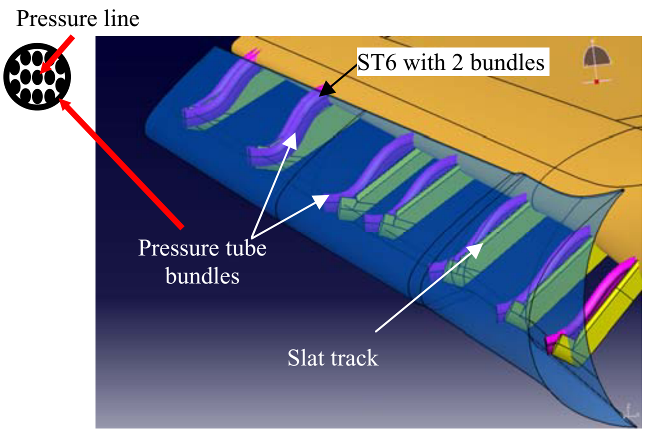

FIG 2. Slat tracks and pressure tube bundles included in the CFD-geometry description.

The main objective of the grid generation is to ensure the same order of the grid influence on the computational results for different configurations. The finite resolution of the grid causes a certain magnitude of the discretization error, which tends to zero as the grid approaches an infinite number of grid points. For practicable computations with EUROLIFT II the total number of grid nodes is limited to be below $20 \cdot 10^6$. Hence special effort is necessary to ensure the prerequisite of the same grid quality for all three configurations.

DLR generated grids using the software package Centaur [4] based on the IGES-formatted surface description exported from CATIA. By placing different sources during the set-up procedure for grid generation the required surface and volume resolution is adjusted. Figure 3 depicts this process in terms of the resulting surface grids.

To capture the strake vortex is essential for the lift breakdown mechanism and thus the achievable level of maximum lift. Spherical sources in combination with a frustrum source are placed along the vortex core which was traced by a first CFD-computation. These sources generate very small isotropic tetrahedral elements slightly growing in size in downstream direction. Figure 4 shows exemplary this placing of sources.

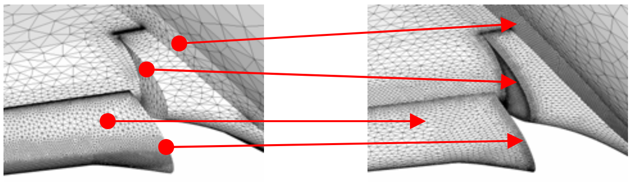

FIG 3. Surface mesh refinement by placing sources.

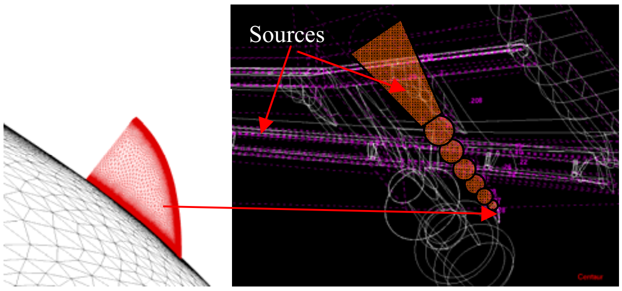

FIG 4. Strake vortex capture by placing sources within Setupgrid of Centaur [4].

The key strategy to fulfill the grid generation objective is to properly place the sources and generate the grid for the most complex configuration, the Stage 3, first. It has to be state that for each configuration a complete re-meshing is necessary. To obtain a grid of the same quality for the next simpler configuration all sources are frozen and only those surface panels are replaced which are affected by the changes in the geometry. In case of the Stage 2 configuration only the nacelle panel which includes the intersection with the strake is exchanged by a panel without strake intersection. All of the strake panels are removed. Since all other panels remain unchanged, the resulting grid after the complete re-meshing consists of the same resolution and quality as the Stage 3 grid.

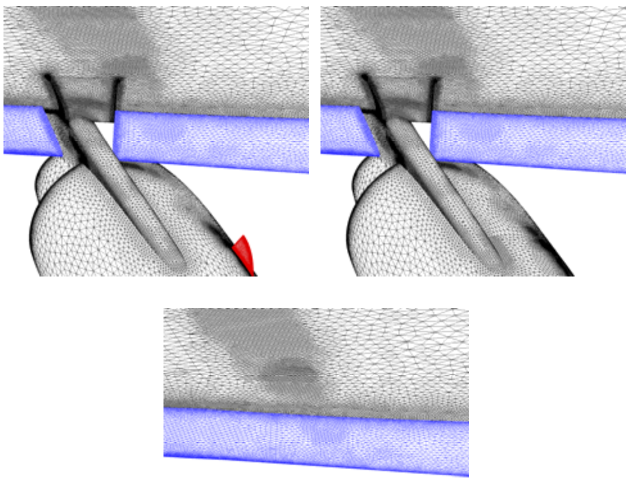

FIG 5. Gradually decreased complexity and frozen sources for the generation of qualitatively equal grid

With this approach DLR generated grids for the LSWT test cases ($Re=1.33\cdot10^6$) as well as for the Stage 3 configuration at $Re=25\cdot10^6$. Within EUROLIFT II the common grids for the ETW test cases ($Re=15\cdot10^6$ and $Re=25\cdot10^6$) were generated by the NLR applying the FASTFLO system [6] for all three configurations. It has to be stated, that for each configuration the grid was used for both ETW Reynolds numbers.

3. TEST CASES AND NUMERICAL METHOD

3.1. Test Cases

The test case matrix of the presented computations is outlined in the following table:

	LSWT		
	$Re=1.33\cdot10^6$ Ma=0.176		
Stage	**1**	**2**	**3**
Test case	**401**	**404**	**407**

	ETW					
	$Re=15\cdot10^6$ Ma=0.202			$Re=25\cdot10^6$ Ma=0.204		
Stage	**1**	**2**	**3**	**1**	**2**	**3**
Test case	**422**	**442**	**462**	**442**	**444**	**464**

TAB 1. Test Case matrix for computations.

Each of the above listed test cases denotes a full polar computation with at least one angle of attack beyond maximum lift. Since within EUROLIFT II these test cases had to be computed by several partners on common grids, the following simplifications and assumptions were made:

- *The flow is treated as fully turbulent for all Reynolds numbers*: Complete transition data for the full range of the polars and for all above listed test cases are not available from experiments or can be predicted within the required accuracy for such complex configurations.
- *Deformation is not considered*: Deformation is unimportant for the LSWT test cases and from reference [5] it is concluded, that deformation has only a secondary effect on maximum lift for the Reynolds number of $Re=15\cdot10^6$. Including deformation would require closed coupled CFD-FEM computations for each angle of attack which was beyond the scope of these activities within EUROLIFT II.
- *Free-flight computations:* The investigations of model installations clearly indicate that the effects on the lift and drag behavior as well as on maximum lift are not negligible [5]. In-tunnel computations are extremely costly in terms of resources and thus beyond the scope of these activities within EUROLIFT II.

3.2. Numerical method

All computations presented in this paper are performed with the DLR TAU flow solver [7]. Central differences are used together with classical dissipation. Turbulent effects are considered by applying the Spalart-Allmaras turbulence model with the Edwards modification [8]. For all computations pre-conditioning is used. Convergence is accelerated by the use of the multi-grid technique and the LUSGS-local time stepping scheme. Close to maximum lift oscillations of the global coefficients are obtained, indicating to a certain extend unsteady flow effects. In such a case the presented values of the global coefficients are averaged through the last 500 cycles.

4. RESULTS

4.1. High-Lift performance prediction

4.1.1. Low Reynolds number cases (LSWT)

The first presented results are the computations of the LSWT-test cases TC401, T404, and TC407. All Cp-distributions which will be presented in the following are taken in the cross sections DV1, DV6 and DV10. The locations are depicted in figure 6.

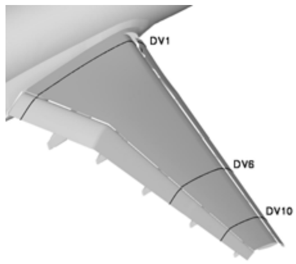

FIG 6. Locations of Cp-measurement cross sections.

In the following figure the computed and measured Cp-distributions are compared at DV1 and DV10 for $\alpha=12.35°$. While at DV10 a good agreement is achieved, deviations are visible for the inboard section DV1.

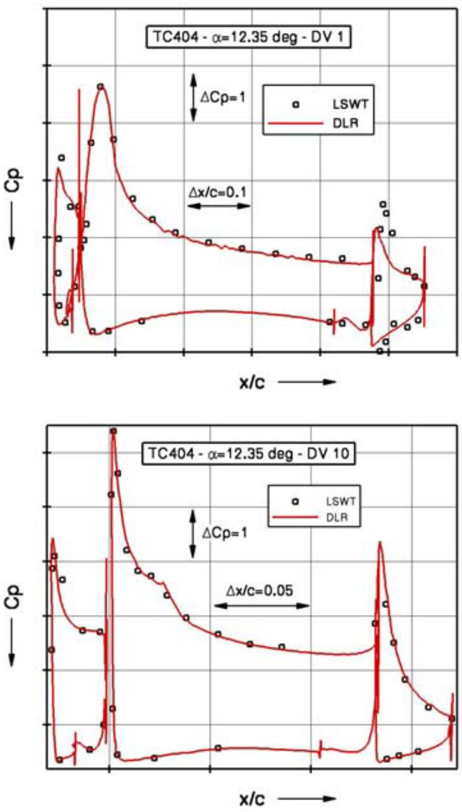

FIG 7. Computed and measured Cp-distributions.

In the LSWT-wind tunnel measurements the model was installed as a half-model. A peniche separates the boundary layer from the fuselage. As outlined in [9] the peniche induces cross-flow velocity components in spanwise direction which lead to an increased loading of the inboard wing section. As the numerical computations are performed in a free-flight set-up, the inboard loading has to be lower as in the half-model measurements. Therefore the DV1 measured Cp-values should be slightly lower especially at the slat compared to the numerical results. However, through the application of suitable wind tunnel correction methods the lift curve and polar should be corrected for these installation effects. Figure 8 shows the computed lift curves for all three configurations cross-plotted with the corrected wind tunnel results.

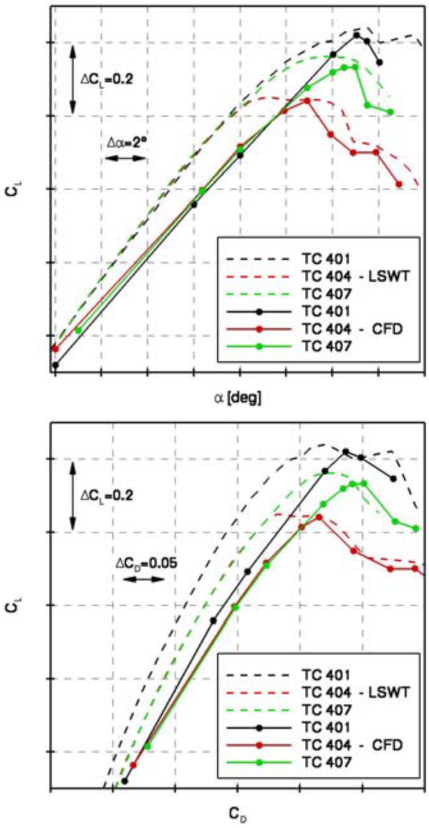

FIG 8. Comparison computed and measured lift curves and polars for all three Stages.

The dashed lines denote the measurements and the solid lines are assigned to the numerical results. For all three Stages the lift seems to be under-predicted in the linear range of the lift curve. Maximum lift on the other hand is predicted within an accuracy of 1.5%. The highest lift and lowest drag are measured for the Stage 1 configuration which also predicted by CFD. With the engine installation a significant loss of maximum lift and an increase in drag are measured. This influence of the engine installation on the global coefficients is captured by the numerical results. As the nacelle strake is added, approximately 60 to 70% of the loss in maximum lift is recovered, which is again very well predicted by CFD. Adding the strake is not producing any noticeable drag increase according to the measurements which is consistently predicted by CFD. It is therefore concluded, that CFD is capable to predict the effect of geometrical changes (Stage 1 to Stage 3) within a good accuracy. However, the direct comparison of the measured and predicted values shows non-negligible differences. The computations seem to under-predict the measured lift coefficient for a given angle of attack and to over-predict drag. According to [10] transition has an only minor effect of the lift curve. Model deformation effects can be neglected due to the atmospheric test conditions and the stiffness of the wind tunnel model. The main reason is considered to be the model installation effects as analyzed in [5]. Additionally, the obtained results con

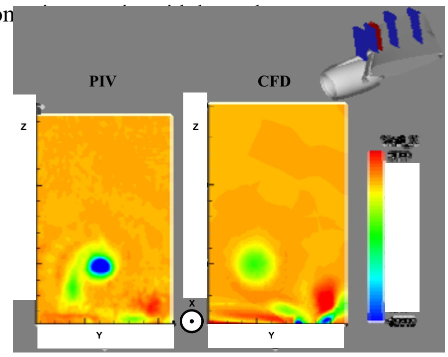

FIG 9. Comparison with PIV at α=16.52°, Stage 3

A further validation result is presented in Figure 9 showing the comparison of the x-vorticity distribution in a plan (PIV-results and computational results for the Stage 3 configuration in terms of the distribution of the x-vorticity component within the red colored plane. The strake vortex is visible in the computational results as a circular vorticity contour. In comparison to the PIV-measurements the location of the vortex in the plane is exactly matched by CFD. The computed vortex strength appears weaker than measured which is caused to some extend by the numerical dissipation and mainly by the production of eddy viscosity inside the vortex. An improvement could be obtained when vortex correction terms in combination with the turbulence model are applied. Figure 10 depicts the computed skin friction lines for the Stage 3 configuration in comparison to flow visualization results obtained during the LSWT tests for the same test case. All main flow features and effects as visible through the skin friction lines are captured by CFD.

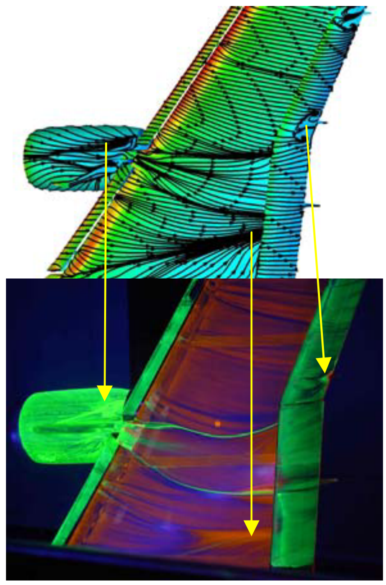

FIG 10. Limiting streamlines at α=18.5°, Stage 3.

From this result and the discussed lift behavior it is concluded that the CFD is well capable to predict the strake effect within good accuracy. The accuracy in predicting the influence of such geometrical differences on the changes of maximum lift underlines further the validity of the applied grid generation strategy.

4.1.2. High Reynolds number cases (ETW)

Typical examples of the obtained level of agreement between computed and measured Cp-distributions in DV1 and DV10 are shown in figure 11 for TC422 at α=16.5°.

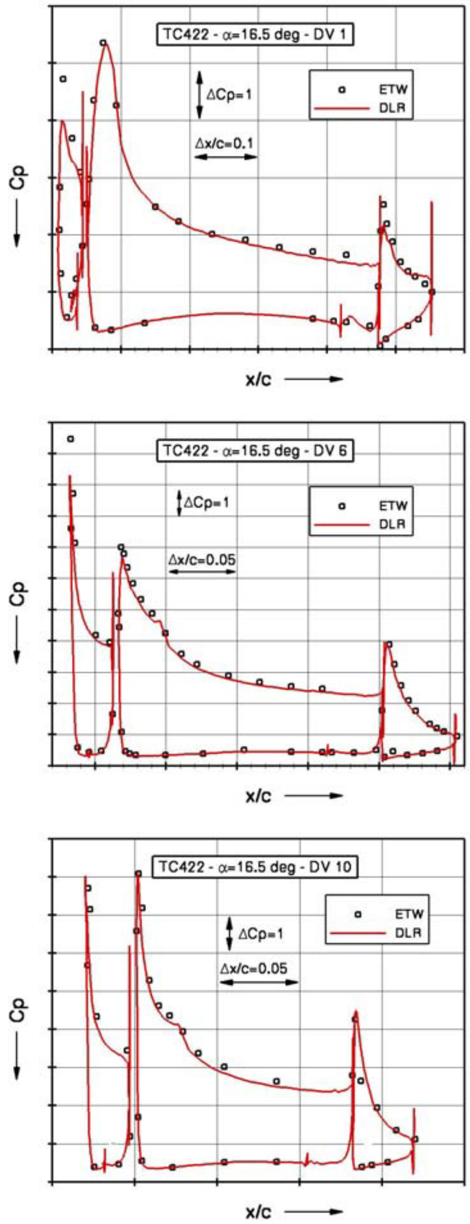

FIG 11. Comparison of Cp-distributions for TC422.

Similar to the previously discussed results the main over-prediction of Cp occurs in the DV1 section. The predicted Cp-distribution at the flap shows a plateau indicating flow separation which is not found in the measurements. A better agreement is obtained in DV6 and DV10, even though the pressure level is not fully captured by CFD. The occurrence of the main deviations to the measurements in the most inboard section of the wing is explained by the induced cross-flow velocities according to [9]. The computed Cp-distributions in DV6 and DV10 show a slight over-prediction of the pressure level on the suction side of the elements. A similar tendency is found for the Stage 2 and Stage 3 test cases for both Reynolds-numbers. Since the model installation effects act mainly inboard of the wing, the existence of a non-negligible grid influence is considered to be the most likely explanation. Other sources of influence such a transition or elastic wing deformation are classified as second order effects according to [5], [10]. Deformation would cause a nose down twist of the main wing which reduces the local angle of attack and would consequently lead to even higher pressure levels (lower Cp-values).

Figure 12 summarises the computed global coefficients in comparison with the measured results in terms of the lift curve and the Lilienthal polar for all three configurations for $Re=25\cdot10^6$.

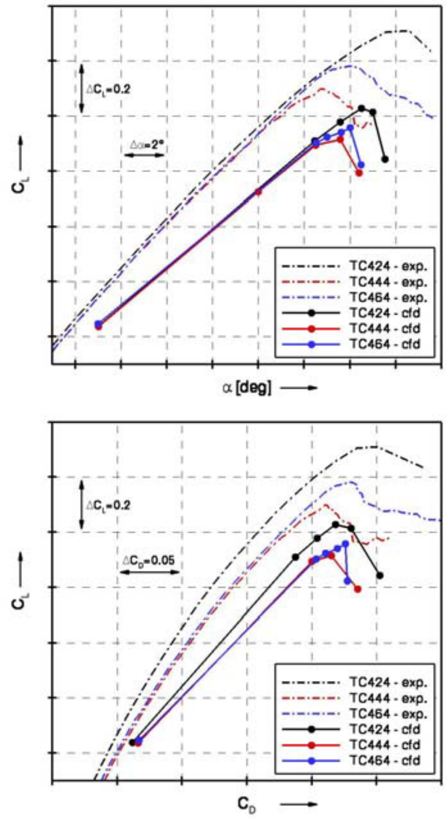

FIG 12. Computed lift curves and polars compared with measurements for all Stages at $Re=25\cdot10^6$.

The Stage 1 configuration (TC424) shows the maximum lift and lowest drag. After engine integration a significant loss of maximum lift is measured. Minor influence is found in the linear part of the lift curve. Adding the installation drag shifts the polar to higher drag values. Different from the LSWT-measurements a very small drag increase is noticeable when the strake is added. This is due to the fact, that the strake itself and the strake position have been optimized at LSWT-conditions. The strake effect itself is less distinct at $Re=25\cdot10^6$ than it is for the LSWT-conditions. At the highest Reynolds number only approximately 50% of the loss of maximum lift could be recovers in the experiments. It is evident from Figure 12, that these geometrical effects as measured in the ETW-wind tunnel are very well predicted by the CFD methods. The differences in maximum lift, the impact on drag and the maximum lift recovery are in a very good agreement to the measurements. A similar match of the measured geometrical effects are obtained for $Re=15\cdot10^6$. Hence, it can be concluded that CFD is very well prepared and capable to predict the impact of geometrical differences within a good accuracy compared to measurements. Similar to the LSWT results it is concluded, that the applied grid generation strategy is very well capable to resolve the influence of the nacelle strake vortex on the lift and drag behavior. On the other hand it has to stated, that further effort is necessary to be capable to predict the absolute values for a single configuration especially for high Reynolds-numbers. Closing this gap is indeed very important for a reliable prediction of maximum lift at true flight conditions.

Of similar importance is the capability of CFD to predict the Reynolds-number influence on maximum lift.

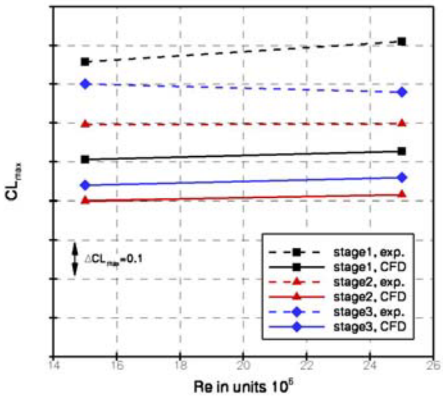

FIG 13. Predicted and measured Reynolds number dependence of maximum lift coefficient.

The measurements are marked with dashed lines and the numerical results with solid lines. Each color is assigned to one configuration. Neglecting the deviation from the measurements as discussed previously a very good qualitative agreement of the Reynolds number dependence is obtained for the Stage 1 and Stage 2 configurations. For the Stage 3 configuration on the other hand CFD predicts the opposite trend to the measurements. Considering the small influence of the Reynolds number ($|\Delta C_{Lmax}|$ = 2 lift counts) and the dependence of the achievable maximum lift on the formation and strengths of the different vortices (see next chapter) the grid resolution might be for this configuration even more important than for the Stage 2 and the Stage 1 configurations.

4.2. Stall mechanisms

The presented results of the global coefficients have shown so far that the CFD methods are capable to predict geometrical differences within a good accuracy. In the following the focus is put on more local effects aiming to assess the prediction capability of the stall mechanism. The wind tunnel measurements provide flow visualization results for selected test cases which serve as basis for the validation of the predicted stall mechanism.

4.2.1. LSWT conditions

From the discussion of the CFD capabilities to predict maximum lift is has been shown, that the value of the measured maximum lift was predicted within an accuracy of 1.5%, but the angle of attack at which maximum lift is obtained is over-predicted up to $\Delta\alpha$=4°. The half model influence, i.e. the induced higher inboard wing loading compared to free-flight conditions, is the main reason identified for this gap in the angle of attack and the slope difference of the lift curves.

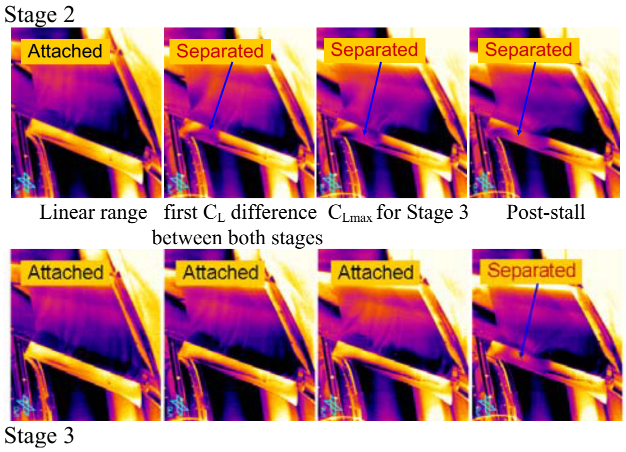

FIG 14. Infra-red pictures of the Stage 2 (top) and the Stage 3 (bottom) from pre-stall (left) to post-stall (right).

In Figure 14 Infra-Red (IR) images for different angles of attack are shown for the Stage 2 configuration (top) and the Stage 3 configuration (bottom). The angle of attack increases from the left to the right. All images focus on the suction side of the inboard slat. In the linear range of the lift curve the flow on the slat is attached for both configurations. As the angle of attack is increased to a point at which first differences in the lift are obtained for both configurations, a slat separation close to the pylon is detected for the Stage 2 configuration whereas the flow retains attached at the Stage 3 slat. When the angle of attack reaches maximum lift of the Stage 3 configuration the Stage 3 slat shows still attached flow and the separation of the Stage 2 slat appears unchanged. In the post-stall region a similar slat separation is now visible for the Stage 3 slat. Hence, the Stage 2 lift breakdown seams to be initiated by the development of a flow separation on the inboard slat. Not visible from the IR images is the flow behavior on the main wing and the flap. A different lift breakdown mechanism appears for the Stage 3 configuration, since the separation on the slat occurs in the post-stall region.

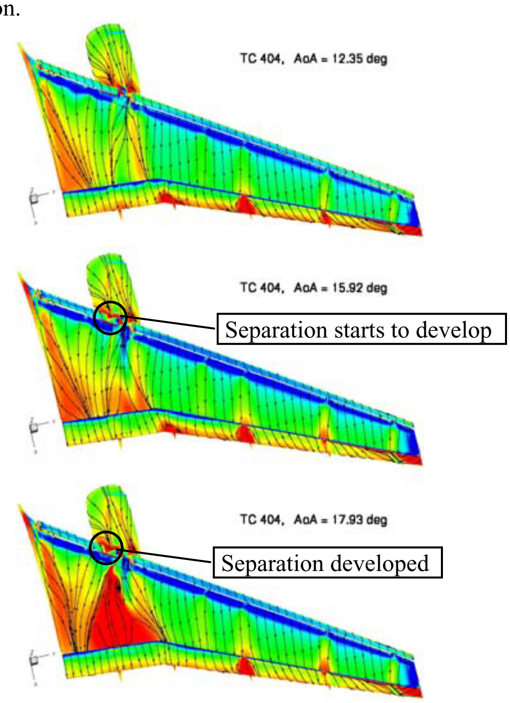

FIG 15. c_{fx}-distributions and skin friction lines for Stage 2.

The computed stall mechanism of the Stage2 configuration is shown in Figure 15. The skin friction lines are plotted on top of the c_{fx}-distribution, which is the distribution of the x-component of the projected skin friction tensor. The red color denotes negative values and thus reversed flow and flow separation. At the lowest angle of attack (Fig. 15 top) parts of the flap in the region of the FTF show small areas of flow separation. The wing root section is attached but the orange color indicates a weakened boundary layer. As the angle of attack increases (Fig. 15 mid) the overall c_{fx}-distribution does not qualitatively change except for the inboard slat and the downstream region of the man wing. A small separation is visible close to the pylon on the inboard slat at exactly the same location as observed in the IR-images. The orange turned color of the c_{fx}-values downstream of the beginning slat separation indicates a weakening of the boundary layer especially at the trailing edge of the main wing. A further increase of the angle of attack leads to a fully developed local slat separation which agrees in terms of its location and size very well to the IR-image. The CFD-results further underline that the lift breakdown is due to the developed large trailing edge separation of the main wing. As the slat separation occurs at an angle of attack at which the main wing flow is attached it is concluded, that the lift breakdown in initiated by local slat separation but the main lift loss comes from the trailing edge separation of the main wing. Latter forms a conical shape and extends upstream to the slat cut-out (see Figure 1). Hence, the CFD-computations predict the same stall mechanism as has been found by IR during the LSWT-wind tunnel measurements.

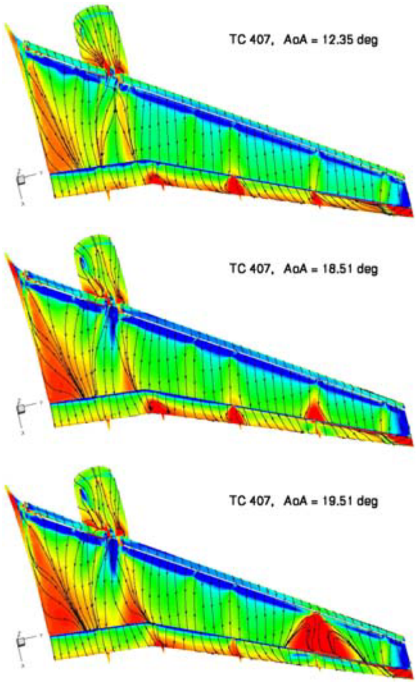

FIG 16. c_{fx}-distributions and skin friction lines for Stage 3.

For the Stage 3 configuration the situation is different. In complete agreement with the IR-images CFD predicts fully attached flow on the inboard slat up to post-stall angles of attack. The flow on the main wing downstream of the inboard slat is attached up to high angles of attack. Here (Fig.15 low) the beginning of a trailing edge separation is indicated. The upstream positioned slat track and pressure tube bundle weaken the boundary layer of the main wing, which tends to separate at the main wing trailing edge. This type of weakening is also found in the c_{fx}-distributions of the Stage 2 configuration at high angles of attack. Up to now all predictions of the flow behavior is in consistence with the wind tunnel results. The main reasons for the lift breakdown predicted by CFD are the development of a wing root separation which starts form the trailing edge and the development of a large outboard flow separation forming a conical shape. The origin of this separation is found to be a large blockage effect from the 6th slat track which is the first slat track with a pressure tube bundle on each side (see Fig. 2). From the measured Cp-distributions in this region a separated flow is indicated but the predicted size is not evident. Two reasons explain these deviations: First, the pressure tubes are solid models of bundles of single small pressure tubes. The flow to some extend is able to pass through the bundle of single tubes in the wind tunnel and hence the blockage effect of the modeled solid replacement body (pressure tube bundle as shown in Fig. 2) might be overestimated. The consequence is a too distinct weakening of the boundary layer of the main wing. Second, the computed free-flight condition shift the wing loading outboard compared to the half model wind tunnel condition at the same lift coefficient. Therefore, the local angles of attack are slightly higher outboard of the wing in free-flight conditions. A further effect could be related to transition. However, the growth of the wing root separation would be even more pronounced when the half model effects are taken into account.

From the presented comparison with the IR-images it is stated, that the main effect of the strake, which is the delay of the slat separation into the post-stall region, is very well captured by CFD. Even though the existence of the large outboard separation at ST6 for the Stage 3 configuration can not be fully proved the dominating mechanisms are captured by CFD. Hence it is concluded that CFD is well capable to predict the associated lift breakdown mechanisms for low Reynolds number conditions.

4.2.2. ETW conditions

The assessment of the capability of CFD to capture the stall mechanisms is more difficult due to the lack of IR-images. Within the ETW tests mini-tufts have been used for imaging the flow close to the surface of the model. Figure 17 depicts an image of mini-tufts exemplary for TC442 (Stage 2) at α=16°.

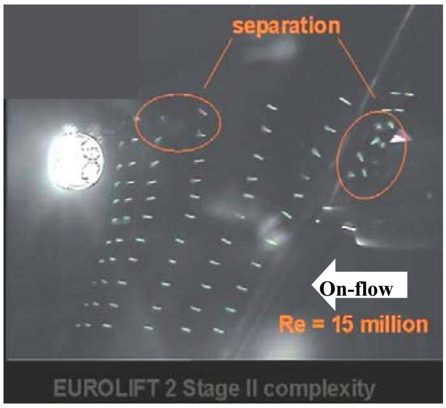

FIG 17. Mini tufts at α=16° for the TC442.

The on-flow direction in this image is from the right and the fuselage is located at the top. A similar flow behavior is observed as for TC404. The inboard slat shows flow separation close to the pylon causing a trailing edge separation of the main wing downstream of the separated slat. Similar images for the Stage 3 configuration show an attached flow on the slat and thus a very similar flow behavior with respect to separation as in the LSWT-cases. It is further found that the Reynolds-number does not alter the stall mechanism.

Figure 18 depicts the computed c_{fx}-distribution and skin friction lines for the Stage 2 configuration at $Re=15\cdot10^6$ and Figure 19 for $Re=25\cdot10^6$.

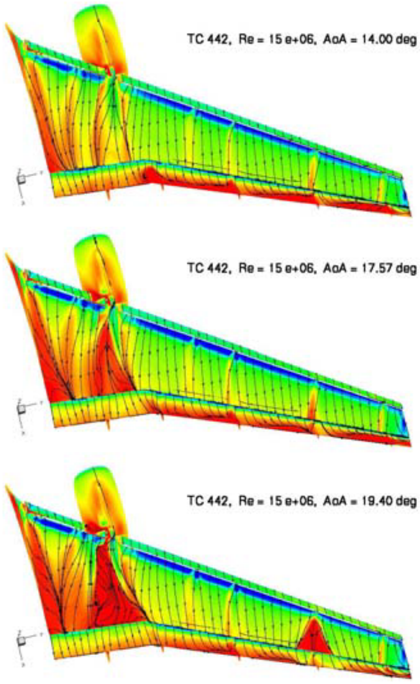

FIG 18. Predicted stall mechanism for Stage 2 at $Re=15\cdot10^6$.

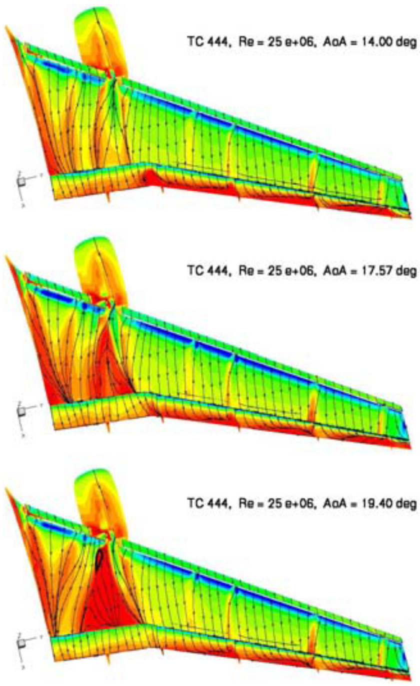

FIG 19. Predicted stall mechanism for Stage 2 at $Re=25\cdot10^6$.

For both Reynolds-numbers the same stall mechanism is obtained. With respect to the limited mini-tuft information a good agreement is found. The main Reynolds-number effect is visible at ST6. For TC442 a conically shaped flow separation is obtained which is vanished for TC444. The dominating stall mechanism is identical to the mechanism described previously for TC404. Therefore underlines the experimental result that the effect of the Reynolds-number on the stall mechanism is negligible. As underlined by the CFD-results even the sizes of the separation regions driving the lift breakdown are almost unaffected by the Reynolds-number which explains the weak Reynolds-number dependence of maximum lift (see Fig. 13).

The strake effect on maximum lift and the stall mechanism has been captured for the LSWT-test case. Figure 20 now shows the stall mechanism predicted for Stage 3 at $Re=25\cdot10^6$.

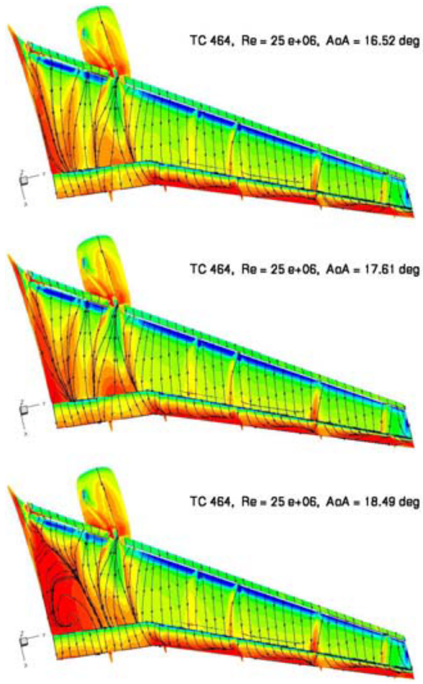

FIG 20. Predicted stall mechanism for Stage 3 at $Re=25\cdot10^6$.

Similar to the LSWT-test cases the flow at the slat stays attached up to the post-stall region. The wing root separation is now much more distinct than in the LSWT-case and its development is evidently the driving mechanism associated with the lift breakdown. Hence, the stall mechanisms for Stage 2 and Stage3 are very different. It has to be stated, that for the Stage 2 configuration a Beret-Basque is not used, neither in the wind tunnel model nor in the CFD-geometry, in order to emphasis the differences in the high-lift vortex system associated with the Stage 2 and the Stage 3 configurations. In real aircraft configurations a Beret-Basque is often used to improve the high-lift performance.

From the above presented results it is concluded, that CFD is very well capable to predict the stall mechanism for high Reynolds numbers. It has also been shown, that the strake effect is very well captured by CFD for each Reynolds number.

The significant differences in the developed vortex systems for the Stage 2 and the Stage 3 configurations are illustrated in Figure 21. Without the strake a strong vortex originating from the nacelle occurs (Fig. 21 top). The colors denote the strength of the x-vorticity component, where the blue color indicates a counter-clockwise rotation of the vortex. The main wing boundary layer is obviously weakened through influence of the strong nacelle vortex. This is indicated by the role up of a vortex structure on the main wing downstream of the separated slat region and rotating in clockwise direction.

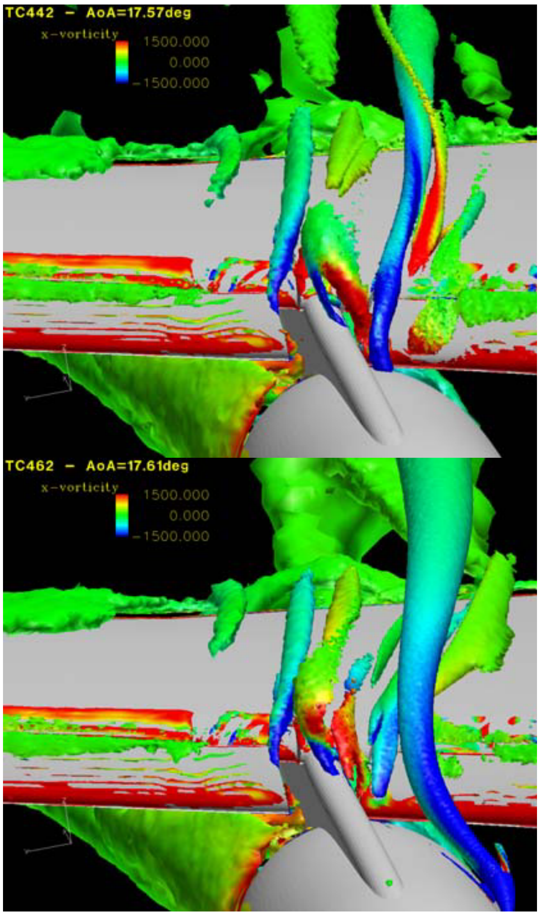

FIG 21. 3D vortex visualization.

As the nacelle strake is added the vortex system changes significantly. The strong nacelle vortex is significantly reduced in strength and has almost vanished. The remains of this vortex are too weak to induce the boundary layer weakening as observed for the Stage 2 configuration. The slat stays attached even at very high angles of attack since the nacelle vortex retains stable in position.

4.3. First results on grid influence

The assessment of the dependence of the numerical result on the resolution and quality of a hybrid grid is difficult. The application of Far-field drag determination methods, exemplary applied to TC442, showed that the amount of spurious drag is below 2% of the total near-field drag [1] which does not close the gap to the measurements. Even though the model installation effect shifts the free-flight lift curves in the direction of the measured curves, the deviation is too high in order to be fully explained. In order to have a first impression on the influence of the grid resolution on the absolute values of the lift coefficient, a new grid for TC462 has been generated using Centaur. In Figure 22 the current grid and the new grid are compared, exemplary at DV6.

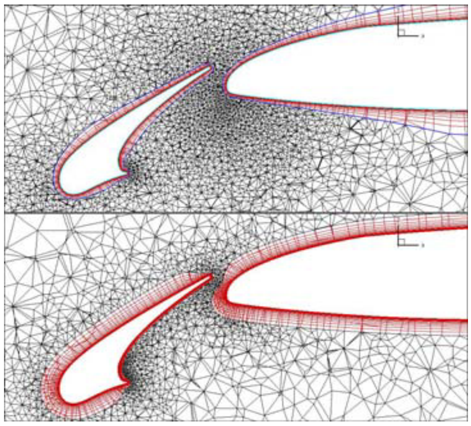

FIG 22. Grid comparison at DV6. New grid at the bottom.

The main difference is the slight increase of the height of the prismatic layers especially at the leading edges of the elements. Especially on the main wing the wake of the slat is transported to a larger extent through the prismatic elements which are less diffusive than the tetrahedral elements. First result in terms of the lift curve is shown in Figure 23.

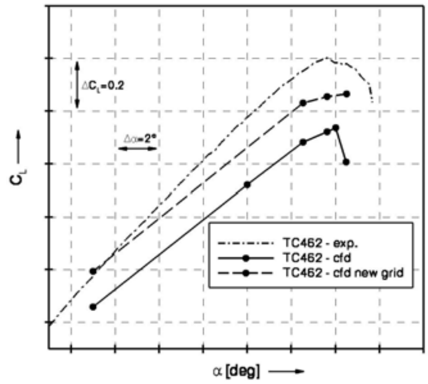

FIG 23. Grid influence on the lift curve.

A significant improve of the predicted lift coefficients is obtained. Even though the measured maximum lift is not yet reached it is clear, that the predicted maximum lift is increase compared to the results of the previous grid. With these encouraging results it is more likely, that the remaining gap to the measured lift curve can be closed when the wind tunnel installation effects are considered. A further analysis of the grid dependence is necessary and attributed to future work. It has to be stated, that the qualitative flow field is not changed, which is important for the following discussions.

4.4. Conclusions

The current paper summarizes the activities of DLR performed within the framework of the European project EUROLIFT II. The KH3Y high-lift configuration has been modified gradually in three Stages towards a complex, realistic high-lift configuration. Extensive numerical computations using the TAU flow solver have been performed for all three configurations at different Reynolds-numbers. The objectives of these activities are the assessment of the CFD capabilities to capture maximum lift for different geometrical complex high-lift configurations, to capture the Reynolds-number dependence of maximum lift, and to improve the understanding for the vortex phenomena associated with the high-lift flows of the different configurations. Within the paper the obtained numerical results have been compared to wind tunnel measurements, conducted within EUROLIFT II for a range of Reynolds-numbers and for all three Stages of the KH3Y configuration. From these comparisons the following conclusions are drawn with respect to the outlined objectives:

- CFD is capable to predict the effect of geometrical details on the lift behaviour and maximum lift.
- The Reynolds-number influence is predicted in qualitative agreement to the wind tunnel measurements.
- The stall mechanisms are captured by CFD.
- The strake effect is predicted within good agreement to the measurements which underlines the validity of the applied grid generation strategy.
- Insights to strake mechanism are obtained by CFD leading to a further understanding of the vortex phenomena and interaction.
- Maximum lift is under-predicted for all computations.
- A significant improvement of the predicted lift curve is obtained with improved prismatic layers, underlining the dependence on the grid resolution and the difficulty to generate high-quality grids with a minimum of grid nodes for high-lift configurations.
- Future work is necessary to identify a best practise approach for a high quality grid generation for high-lift configurations.
- Future work necessary to include installation effects by cost intensive in-tunnel computations

In a constitutive next step all the lessons learned with respect to transition, the geometrical effects, deformation, and half-model effects have to be combined in a final validation step, i.e. a final numerical prediction exercise in which all aspects are considered at the same time. This final validation would quantify the remaining uncertainties. Especially the uncertainty of the grid dependence of the obtained results has to be analysed and addressed in future work.

Acknowledgments

The research work discussed in this paper was performed within the European project EUROLIFT II (European High-Lift Programme II) as part of the 6th European Framework Programme, which is co-financed by the European Commission under the contract number AST-2004-502896.

4.5. References

[1] Frhr. von Geyr, H. et al. „CFD Prediction of the Maximum Lift Effects on Realistic High Lift Commercial Aircraft Configurations within the European Project EUROLIFT II", *25th AIAA Applied Aerodynamics Conference*, AIAA 2007-4299, Miami, Florida, USA, June 25-28, 2007 (to be published).

[2] Smith, A.M.O. "High-Lift Aerodynamics", 37th Wright Brothers Lecture, AIAA Paper No. 74-939, *AIAA 6th Aircraft Design, Flight Test and Operations Meeting*, Los Angeles, CA, August 12-14, 1974.

[3] CATIA V5, Release R14, Dassault Systems, http://www.3ds.com

[4] Centaur, Release 6.0.3, CentaurSoft™, http://www.centaursoft.com

[5] Van der Burg, J.W. et al. "Geometrical Model Installation and Deformation Effects in the EUROPEAN Project EUROLIFT II", *25th AIAA Applied Aerodynamics Conference*, AIAA 2007-4297, Miami, Florida, USA, June 25-28, 2007 (to be published).

[6] Van der Burg, J.W., van der Heul, D., Schippers, H. "Experiences with unstructured grid coarsening for conformal antennas", *Proceedings of the 9th International Conference on Numerical Grid Generation in Computational Field Simulations*, San Jose, USA, June 2005.

[7] Gerhold, T. "Overview of the Hybrid RANS Code TAU", *Notes on Numerical Fluid Mechanics and Multidisciplinary Design*, Vol. 89, ISBN 3-540-24383-6, pp. 81-92.

[8] Spalart P.R. and Allmaras S.R. "A one-equation turbulence model for aerodynamic flows", Paper 92-0439, AIAA, 1992.

[9] Eliasson, P. "Numerical validation of half model high-lift configuration in a wind tunnel", *45th AIAA Aerospace Science Meeting and Exhibit*, AIAA-2007-262, Reno, Nevada, USA, January 2007.

[10] Moen, F. et al. "Transition prediction and impact on 3D high-lift wing configuration", *AIAA 25th Applied Aerodynamics Conference*, AIAA-2007-4302 Miami, FL, June 25-28, 2007.